4

Multiscale finite element methods using limited global information

4.1 Motivation

Previously, we discussed multiscale methods that employ local information in computing basis functions. The accuracy of these approaches depends on local boundary conditions. Although effective in many cases, multiscale methods that only use local information may not accurately capture the solution at all scales. In particular, in regions with no scale separation, the local multiscale methods cannot accurately approximate the scales that are comparable to the computational coarse-grid size. A rich hierarchy of scales can introduce an important connectivity at different scales that need to be captured at larger scales. The natural question is how to incorporate the information from different scales into localized multiscale basis functions such that the resulting numerical solution provides an accurate approximation of the global solution.

In this chapter, we discuss how to take into account the information that is not captured by local basis functions. We call this information global information although it can be information in some large regions where important connectivity of the media may occur. For example, subsurface properties often do not have scale separation and high/low conductivity regions can be connected at various scales (e.g., Figures 1.2–1.4). The connectivity regions are often very complicated due to conductivity variations within these regions and their complex geometrical structures. Similar situations can occur in composite materials where the material properties can vary at different scales. These complex features are often incorporated into global fields which are used to construct localized multiscale basis functions. In this chapter, we discuss the concept of global multiscale methods and their applications.

We demonstrate the main idea of global multiscale methods on the example of porous media flow, although this concept can be generalized to many other applications such as composite materials. Consider

$$- \operatorname{div}(\lambda(x)k(x)\nabla p) = f, \tag{4.1}$$

where $k(x)$ is a heterogeneous field and $\lambda(x)$ is assumed to be a smooth field. This equation is derived from two-phase flow equations when gravity and capillary effects are neglected (see Section 2.10). Our goal is to construct multiscale basis functions on the coarse grid (with grid size larger than the characteristic length scale of the problem) such that these basis functions can be used for various source terms $f(x)$, boundary conditions, and mobilities $\lambda(x)$. Here, $k(x)$ does not have scale separation and has a multiscale structure that may not be captured accurately via local basis functions.

In order to capture the multiscale structure of the media at different scales, one needs to embed the multiscale information into the global fields. More precisely, we assume that the solution can be represented by a number of fields $p_1, ..., p_N$, such that

$$p \approx G(p_1, ..., p_N), \tag{4.2}$$

where G is a sufficiently smooth function, and $p_1, .., p_N$ are global fields. These fields typically contain the essential information about the heterogeneities at different scales and can also be local fields (see discussion below). In the above assumption (4.2), p_i are solutions of elliptic equations. For the mixed MsFEM, one can formulate an assumption similar to (4.2) for velocities. We denote by $v_i = -k\nabla p_i$. Then, the above assumption can be written in the following way. There exist sufficiently smooth scalar functions $A_1(x), ..., A_N(x)$, such that the velocity corresponding to (4.1) ($v = -\lambda(x)k(x)\nabla p$) can be written as

$$v \approx A_1(x)v_1 + \cdots + A_N(x)v_N. \tag{4.3}$$

Note that it is important that G (or A_1, ..., A_N) are smooth functions so that the multiscale basis functions which span $p_1, ..., p_N$ (or $v_1, ..., v_N$) can accurately approximate the global solution. More details on the assumption on $A_1, ..., A_N$ or G are formulated later.

For problems without scale separation, the functions $p_1, ..., p_N$ are often the solutions of global problems or their approximations. These methods are effective when (4.1) is solved multiple times. For problems with scale separation, one can use the solutions of the local problems in constructing multiscale basis functions. We note that when only local information is used, one still needs (4.2) (or (4.3) for fluxes) in each coarse-grid block to guarantee that the local solutions can approximate the global solution in each coarse patch. Once these global fields are determined, the multiscale basis functions are constructed such that they span these global fields. Thus, the multiscale methods with limited global information can be regarded as an extension of MsFEM discussed in Chapter 2. One of the main challenges is to determine the global fields. This is discussed next.

In a general setting, it was shown by Owhadi and Zhang [218] that for an arbitrary smooth $\lambda(x)$, the solution of (4.1) is a smooth function of d linearly independent solutions of single-phase flow equations ($N = d$), where d is the space dimension. These results are shown under some suitable assumptions for

the case $d = 2$ and more restrictive assumptions for the case $d = 3$. In [103], it was shown that for channelized permeability fields, p is a smooth function of single-phase flow pressure (i.e., $N = 1$), where the single-phase pressure equation is described by $\mathrm{div}(k\nabla p^{sp}) = 0$ with boundary conditions as those corresponding to two-phase flow. Multiple global fields can be used for the system of equations or for the random coefficients. For the system of equations, these global fields are the solutions of the homogeneous system subject to boundary conditions $(0, ..., x_i, ..., 0)$ $(i = 1, ..., d)$, where x_i is chosen for each component of the vector field solution and zero otherwise (as in homogenization; see [28]). When considering random permeability fields, the permeability field is typically parameterized with a parameter that represents the uncertainties. In this case, we deal with a family of heterogeneous permeability fields such as $k = k(x, \theta)$, where θ is in a high-dimensional space. For example, log-Gaussian permeability fields can be characterized using Karhunen–Loéve expansion (e.g., [182]) as

$$k(x, \theta_1, ..., \theta_M) = \exp(\sum_i \theta_i \Phi_i(x)),$$

where $\Phi_i(x)$ are pre-computed spatial fields that depend on a covariance matrix associated with k. In many of these parameterized cases, $k(x, \theta)$ is a smooth function of $\theta = (\theta_1, ..., \theta_M)$, and thus one can use the solutions corresponding to a few realizations of k to represent the heterogeneities across the ensemble (see Section 5.7.1).

4.1.1 A motivating numerical example

In this section, we present a numerical example where the use of local boundary conditions does not perform well and there is a need to use some type of global information. We consider the two-phase immiscible flow and transport setting presented in Section 2.10 with quadratic relative permeability functions and neglect the effects of gravity and capillarity. Multiscale methods generally perform well for permeability fields generated using two-point correlation functions (e.g., [85]). However, the local multiscale methods do not perform well in the presence of strong nonlocal effects as do those that appear in channelized permeability fields. In our numerical example, we consider strongly channelized permeability fields, and in particular, show that the local basis functions cannot accurately capture the global effects. These permeability fields have been proposed in some recent benchmark tests, such as the Tenth SPE Comparative Solution Project [78].

In Figure 4.1, one of the layers of this 3D permeability field is depicted. All the layers have 60×220 fine-scale resolution, and we take the coarse grid to be 6×22. As can be observed, the permeability field contains a high-permeability channel, where most flow occurs in our simulation. In Figure 4.2, the saturation fields at time PVI = 0.5 are compared (see (2.44) for the definition
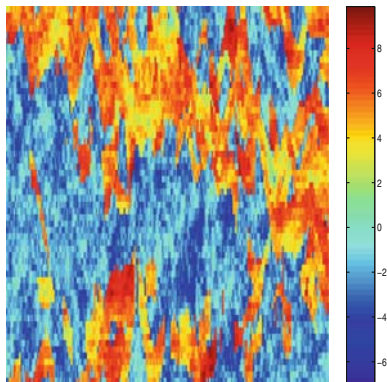
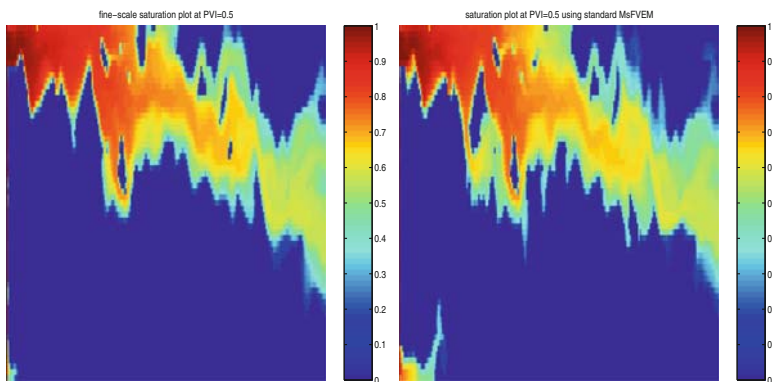**Fig. 4.1.** Log-permeability for one of the layers of upper Ness.

Fig. 4.2. Saturation maps at PVI = 0.5 for fine-scale solution (left figure) and standard MsFVEM (right figure).

of PVI). We use the MsFVEM as described in Section 2.10, where the elliptic equation is solved on the coarse grid, whereas the transport equation is solved on the fine grid with the fine-scale velocity field re-constructed using multiscale basis functions. Thus, the errors are due to the MsFVEM only. We see that MsFVEMs with local basis functions introduce some errors. In the bottom left corner, there is a saturation pocket that is not in the reference solution computed using the fine grid. This is because the local basis functions in the lower-left corner contain a high permeability region. However, this high permeability region does not have global connectivity, and the local basis functions cannot take this effect into account. Next, we discuss how global information can be incorporated into multiscale basis functions to improve the accuracy of the computations. Later in the book, we show that some more general multiphase flow and transport numerical results can be improved by using limited global information.

4.2 Mixed multiscale finite element methods using limited global information

4.2.1 Elliptic equations

In this section, we study mixed MsFEMs that employ global information. We consider elliptic equations with Neumann boundary conditions

$$
\begin{aligned}
-\mathrm{div}(\lambda(x)k(x)\nabla p) &= f(x) \quad \text{in} \quad \Omega \\
\lambda(x)k(x)\nabla p \cdot n &= g \quad \text{on} \quad \partial\Omega,
\end{aligned}
\tag{4.4}
$$

where $k(x)$ is a heterogeneous field and $\lambda(x)$ is a smooth field, as before. We assume that $\int_\Omega p\,dx = 0$. Denote by $v = -\lambda(x)k(x)\nabla p$ the velocity. To construct basis functions for a global mixed MsFEM, we assume that the velocity field v can be approximated by a priori defined global velocity fields, $v_1, ..., v_N$ in the following way. There exist functions $v_1, ..., v_N$ and $A_1(x), ..., A_N(x)$ such that

$$
v(x) \approx \sum_{i=1}^{N} A_i(x)v_i(x),
\tag{4.5}
$$

where $A_i(x)$, $i = 1, ..., N$, are sufficiently smooth. The assumption (4.5) is made more precise in Section 6.3. We note that $v_i = -k\nabla p_i$ are, in general, solutions of $\mathrm{div}(k\nabla p_i) = 0$, $v_i = -k\nabla p_i$, with some boundary conditions. In (4.5), we assume that the velocity field in each coarse-grid block can be approximated by a linear combination of a priori defined velocity fields.

Next, we construct the multiscale velocity basis functions using the information from $v_1, ..., v_N$. The main difference between this construction and the construction presented in Section 2.5.2 is the use of oscillatory boundary conditions that depend on $v_1, ..., v_N$. Specifically, we construct the basis functions for the velocity field as follows:

$$
\begin{aligned}
\mathrm{div}(k(x)\nabla \phi_{ij}^K) &= \frac{1}{|K|} \quad \text{in} \quad K \\
k\nabla\phi_{ij}^K \cdot n &= \begin{cases} \frac{v_i \cdot n}{\int_{e_j} v_i \cdot n\,ds} & \text{on } e_j^K \\ 0 & \text{else,} \end{cases}
\end{aligned}
\tag{4.6}
$$

where $\int_K \phi_{ij}^K dx = 0$, $i = 1, ..., N$, $j = 1, ..., j_K$ (j_K is the number of edges or faces of K), and e_j^K are edges (or faces in $\mathbb{R}^3$) of K. In Figure 4.3, we schematically illustrate the basis function construction. Let $\psi_{ij}^K = k(x)\nabla\phi_{ij}^K$. We define the finite-dimensional space spanned by these basis functions by

$$
\mathcal{V}_h = \mathrm{span}\{\psi_{ij}^K\}.
$$

We denote by $\mathcal{V}_h^0$ the span of ψ_{ij}^K that satisfies homogeneous Neumann boundary conditions. We set Q_h to be piecewise constant basis functions that are used to approximate the pressure p, as in Section 2.5.2.

As in Section 2.5.2, we can combine the basis functions in adjacent coarse-grid blocks with a common edge e_j and obtain the multiscale basis function for the edge e_j denoted by ψ_{ij}. Let K_1 and K_2 be adjacent coarse grid blocks. Then ψ_{ij} solves (4.6) in K_1 and solves $\text{div}(\psi_{ij}) = -1/|K_2|$ in K_2, and $\psi_{ij} \cdot n = -v_i \cdot n / \int_{e_j^K} v_i \cdot n ds$ on $e_j^{K_2}$ and 0 otherwise. In other words, $\psi_{ij} = \psi_{ij}^{K_1}$ in K_1 and $\psi_{ij} = -\psi_{ij}^{K_2}$ in K_2, where ψ_{ij}^K is defined via the solution of (2.16) (cf. Figure 2.8 for the illustration).

Let $\{v_h, p_h\}$ be the numerical approximation of $\{v, p\}$ with the basis functions defined previously. The numerical mixed formulation of (4.4) is to find $\{v_h, p_h\} \in \mathcal{V}_h \times Q_h$ such that

$$\int_\Omega (\lambda k)^{-1} v_h \cdot w_h dx - \int_\Omega \text{div}(w_h) p_h dx = 0 \quad \forall w_h \in \mathcal{V}_h^0$$
$$\int_\Omega \text{div}(v_h) q_h dx = \int_\Omega f q_h dx \quad \forall q_h \in Q_h. \tag{4.7}$$

The discrete formulation corresponding to the resulting system is similar to (2.18).

Note that for each edge, we have N basis functions and we assume that $v_1, ..., v_N$ are linearly independent in order to guarantee that the basis functions are linearly independent. To ensure the boundary condition in (4.6) is well defined, we assume that $\int_{e_l^K} v_i \cdot n ds$ is not zero. To avoid the possibility that $\int_{e_l^K} |v_i \cdot n| ds$ is unbounded, we need to make certain assumptions that bound $\int_{e_l^K} |v_i \cdot n| ds$ from above. These assumptions are formulated in Section 6.3.

In Section 6.3, it is shown that the MsFEM using limited global information converges without any resonance error. We present numerical results in the next section as well as in Section 5.7.1 to demonstrate the importance of the use of global information.

Remark 4.1. We note that local mixed MsFEMs introduced in Section 2.5.2 can be obtained from mixed MsFEMs introduced in this section. To do this, one needs to use one global field v_1 which is a constant vector and $v_1 \cdot n \neq 0$ along each edge e. Taking into account that $v_1 \cdot n$ is constant along each edge, we have $v_1 \cdot n / \int_e v_1 \cdot n ds = 1/|e|$. This is the same as the boundary conditions introduced for local problems in Section 2.5.2.

Remark 4.2. The representative coarse grid K can be nonconvex (c.f., Figure 4.3). The analysis presented in Section 6.3 implies that the global mixed multiscale finite element method works for nonconvex meshes. Strongly stretched meshes can have an impact on the convergence rate of the method following the analysis in Section 6.3.

Remark 4.3. The construction of velocity basis functions in (4.6) and the analysis in Section 6.3 imply that K is not necessarily a polygon domain and the interface normal can be a spatial function.
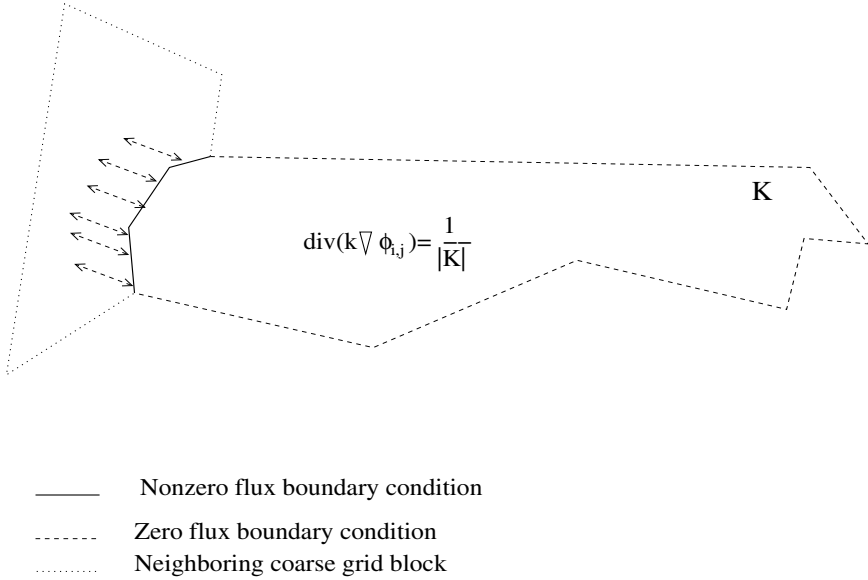
$$\text{div}(k\nabla \phi_{i,j}) = \frac{1}{|K|}$$

_____ Nonzero flux boundary condition

------- Zero flux boundary condition

.... Neighboring coarse grid block

Fig. 4.3. Schematic description of velocity basis function construction.

Remark 4.4. We note that the global mixed MsFEMs presented in the book can be used when meshes have hanging nodes and when fine grids do not necessarily match across coarse grid interfaces.

Pseudo-code. Next, we briefly outline the implementation of mixed Ms-FEMs. We note that the implementation of mixed MsFEMs is similar to Algorithm 2.5.2, except one needs to compute or obtain global fields. Note that global fields can be defined iteratively (see Section 4.4). We have posted simple prototype MATLAB codes for solving elliptic equations with mixed MsFEMs (courtesy of J.E. Aarnes) at
$http://www.math.tamu.edu/ \sim yalchin.efendiev/codes/.$

4.2.2 Parabolic equations

Mixed MsFEMs using limited global information can be easily extended to parabolic equations. We consider the following model parabolic equation,

$$\begin{aligned}
\frac{\partial}{\partial t}p - \text{div}(\lambda(x)k(x)\nabla p) &= f(x,t) \quad \text{in} \quad \Omega \times [0,T] \\
p &= 0 \quad \text{on} \quad \partial\Omega \times [0,T] \\
p(t=0) &= p(0) \quad \text{in} \quad \Omega,
\end{aligned} \tag{4.8}$$

where $k(x)$ is a bounded symmetric and positive definite matrix in Ω, and $p(0)$ is a smooth spatial field. Denote by $v = -\lambda(x)k(x)\nabla p$.

Algorithm 4.2.1

Set coarse mesh configuration from fine-scale mesh information.
Define global fields $v_1, ..., v_i, ..., v_N$ used in the simulations.
For each coarse-grid block n and for each global field i do
  – For each edge j of a coarse-grid block
  – Solve for ψ_{ij}^n according to (4.6)
  – End for
End do.
Assemble the coarse-scale system according to (4.7).
Assemble the external force on the coarse mesh according to (4.7).
Solve the coarse-grid formulation.

For parabolic equations, we assume that the velocity v can be approximated by multiple global fields. In particular, we assume that there exist $v_1, ..., v_N$ and sufficiently smooth functions $A_1(t, x), ..., A_N(t, x)$ such that

$$v(t, x) \approx \sum_{i=1}^{N} A_i(t, x)v_i(x).$$

This assumption is made more precise in Section 6.3.1.

The mixed formulation associated with (4.8) is to find $\{v, p\}$ such that

$$\int_\Omega \frac{\partial}{\partial t} p \, q dx + \int_\Omega \mathrm{div}(v) \, q dx = \int_\Omega fq \quad \forall q \in L^2(\Omega)$$
$$\int_\Omega (\lambda k)^{-1} v \cdot w dx - \int_\Omega \mathrm{div}(w) \, p dx = 0 \quad \forall w \in H(\mathrm{div}, \Omega) \quad (4.9)$$
$$p(t = 0) = p(0).$$

Let finite-dimensional space $\mathcal{V}_h$ and Q_h be defined as in the elliptic case. The space-discrete mixed formulation is to find $\{v_h, p_h\} : [0, T] \longrightarrow \mathcal{V}_h \times Q_h$ such that

$$\int_\Omega \frac{\partial}{\partial t} p_h q_h dx + \int_\Omega \mathrm{div}(v_h) \, q_h dx = \int_\Omega fq_h dx \quad \forall q_h \in Q_h$$
$$\int_\Omega (\lambda k)^{-1} v_h \cdot w_h dx - \int_\Omega \mathrm{div}(w_h) \, p_h dx = 0 \quad \forall w_h \in \mathcal{V}_h \quad (4.10)$$
$$p_h(t = 0) = p_{0,h},$$

where $p_{0,h}$ is the L^2 projection of $p(0)$ onto Q_h. This problem can be also re-written in matrix form

$$A \frac{\partial}{\partial t} P + BU = F$$
$$B^T P - DU = 0 \quad (4.11)$$

with $P(0)$ given, where A and D are symmetric positive and definite. After eliminating U, (4.11) is a linear system ODE for P,

$$A\frac{\partial}{\partial t}P + BD^{-1}B^T P = F.$$

The analysis of the method is presented in Section 6.3.

4.2.3 Numerical results

The use of single global information

In our numerical simulations, we perform two-phase flow and transport simulations with the same setting as before, except we assume that the source terms (q_t in (2.40)) are given by a standard five-spot problem (see e.g., [1]), where the injection well is placed at the middle and the four production wells are placed at four corners of the rectangular global domain. We assume no flow along the boundaries. Initially, it is assumed that $S = 0$ in the whole domain. In the simulations, we solve the pressure equation on the coarse grid and reconstruct the fine-scale velocity field which is used to solve the saturation equation. The fine-scale velocity is reconstructed simply by using the multiscale basis function as

$$v = \sum_e v_e \psi_e,$$

where the sum is taken over all edges e (or faces), v_e is the coarse-scale normal velocity field for edge e obtained via the solution of mixed MsFEMs, and ψ_e is the velocity basis function for edge e. If there are several multiscale basis functions for each edge, then

$$v = \sum_{e,i} v_{e,i} \psi_{e,i},$$

where i corresponds to the global field v_i (see (4.3)). Because we use a reconstructed fine-scale velocity field, the errors will be due to mixed MsFEMs only. The basis functions are constructed at time zero and not changed throughout the simulations. As for permeability fields, we use heterogeneous permeability fields from the Tenth SPE Comparative Solution Project [78] (also referred to as SPE 10). Because of channelized structure of the permeability fields, the localized approaches do not perform well, as we observed earlier. On the other hand, the use of limited global information based on single-phase flow information improves the accuracy.

We first present numerical results where one global field (single-phase flow solution) is used ($N = 1$ in (4.3)). More precisely, $\text{div}(k\nabla p_1) = q_t$, where q_t represents the source terms corresponding to the five-spot problem and $v_1 = -k\nabla p_1$. We compare a mixed MsFEM with limited global information and a

mixed MsFEM which uses only local information. In Tables 4.1–4.6 numerical
results for different layers of SPE 10 using different viscosity ratios (see (2.39))
and different coarse grid sizes are shown. In these tables, the L^1 saturation
errors over the time interval from 0 to 1 PVI as well as fractional flow errors are
compared. It is evident from these tables that a mixed MsFEM using limited
global information performs much better than a mixed MsFEM which only
uses local information. Moreover, we observe that a mixed MsFEM converges
as the mesh size decreases. We present saturation snapshots in Figure 4.4.
These results indicate that for general complicated media such as SPE 10
with high contrast, one can expect the convergence of a mixed MsFEM as the
coarse mesh size decreases when using limited global information.

Table 4.1. Relative Errors (Layer 40, $\mu_o/\mu_w = 3$)

Coarse Grid	Frac. Flow Error (Global)	Saturation Error (Global)	Frac. Flow Error (Local)	Saturation Error (Local)
6×10	0.0144	0.0512	0.1172	0.2755
12×22	0.0039	0.0370	0.1867	0.3158

Table 4.2. Relative Errors (Layer 50, $\mu_o/\mu_w = 3$)

Coarse Grid	Frac. Flow Error (Global)	Saturation Error (Global)	Frac. Flow Error (Local)	Saturation Error (Local)
6×10	0.0129	0.0871	0.1896	0.5061
12×22	0.0046	0.0568	0.1702	0.4578

Table 4.3. Relative Errors (Layer 70, $\mu_o/\mu_w = 3$)

Coarse Grid	Frac. Flow Error (Global)	Saturation Error (Global)	Frac. Flow Error (Local)	Saturation Error (Local)
6×10	0.0106	0.0562	0.0408	0.2291
12×22	0.0039	0.0421	0.0976	0.2530

Mixed MsFEM on unstructured grids and the coupling to coarse-scale transport equation

In [4], the mixed MsFEM is used for simulations on unstructured coarse grids.
The use of unstructured coarse grids has advantages in subsurface simula-
tions because they provide flexibility and can render more accurate upscaled

Table 4.4. Relative Errors (Layer 40, $\mu_o/\mu_w = 10$)

Coarse Grid	Frac. Flow Error (Global)	Saturation Error (Global)	Frac. Flow Error (Local)	Saturation Error (Local)
6×10	0.0080	0.0534	0.0902	0.2721
12×22	0.0026	0.0403	0.1414	0.3153

Table 4.5. Relative Errors (Layer 50, $\mu_o/\mu_w = 10$)

Coarse Grid	Frac. Flow Error (Global)	Saturation Error (Global)	Frac. Flow Error (Local)	Saturation Error (Local)
6×10	0.0049	0.0957	0.1577	0.5137
12×22	0.0041	0.0628	0.1404	0.4613

Table 4.6. Relative Errors (Layer 70, $\mu_o/\mu_w = 10$)

Coarse Grid	Frac. Flow Error (Global)	Saturation Error (Global)	Frac. Flow Error (Local)	Saturation Error (Local)
6×10	0.0044	0.0629	0.0280	0.2262
12×22	0.0025	0.0473	0.0678	0.2397

solutions for flow and transport equations. It is often necessary to use an unstructured coarse grid when highly heterogeneous reservoirs are discretized via irregular anisotropic fine grids. Our study is motivated by the development of coarse-scale models for coupled flow and transport equations in a multiphase system. An unstructured coarse grid is often used to upscale the transport equation with hyperbolic nature in a highly heterogeneous reservoir. Solving the flow equation on the same coarse grid provides a general robust coarse-scale model for the multiphase flow and transport at a low CPU cost. We note that most of the previous studies employ a two-grid approach where the flow equation is solved on a coarse grid and the transport equation is solved on a fine grid. We consider the nonuniform coarsening developed in [9] for the transport equation (also described in Section 5.5). The coarse grid we obtain is highly anisotropic and is not quasi-uniform. We present numerical results when both the flow and transport equations are solved on the coarse grid. In [4], numerical examples involving highly channelized permeability as well as a 3D reservoir model using an unstructured fine grid are presented. Next, we present a few numerical examples.

For our numerical example, we consider layer 65 of SPE 10. Using the algorithm for upscaling of the transport equation ([9]), we generate a coarse grid. In Figure 4.5, the fine-scale permeability and the coarse grid are plotted. In Figure 4.6, we present the results for the saturation fields at PVI= 1 when both the flow and the transport equations are solved on the coarse grid. One can see from this figure that the saturation profile looks realistic when an adaptive coarse grid is used and we preserve the geological realism reasonably
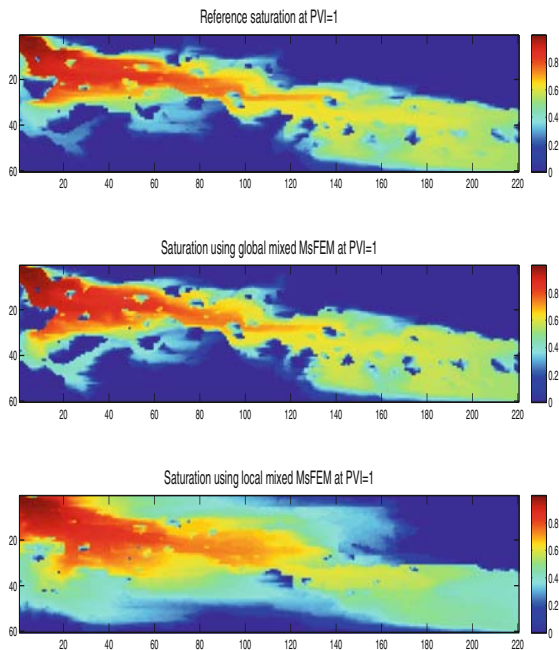
Fig. 4.4. Comparison of saturation fields between reference solution and MsFEM solution at PVI $= 1$, layer 50, 12×11 coarse grid and $\mu_o/\mu_w = 10$; top: reference saturation; middle: saturation using global mixed MsFEM; bottom: multiscale saturation using local mixed MsFEM.

well. In Table 4.7 we present L^1 relative errors for the saturation when different resolutions of the coarse grid are used. In the same table, we show the errors corresponding to the structured grids with a comparable number of coarse-grid blocks (shown in parentheses). We can make two important observations from this table. First, the errors are small (less than 1%). Second, the mixed MsFEM on an unstructured grid performs better. The latter is due to the fact that the unstructured grid is constructed using some relevant limited global information which usually increases the accuracy of the method.

In our next numerical example, we test the method on a synthetic reservoir with a corner-point grid geometry. The corner-point grid has vertical pillars, as shown in Figure 4.7, 100 layers, and 29,629 active cells (cells with positive volume). The permeability ranges from 0.1 mD to 1.7 D and the porosity is assumed to be constant. The corner-point grid (or pillar grid) format [231] is a very flexible grid format that is used in many commercial geomodeling softwares. Essentially a corner-point grid consists of a set of hexahedral cells
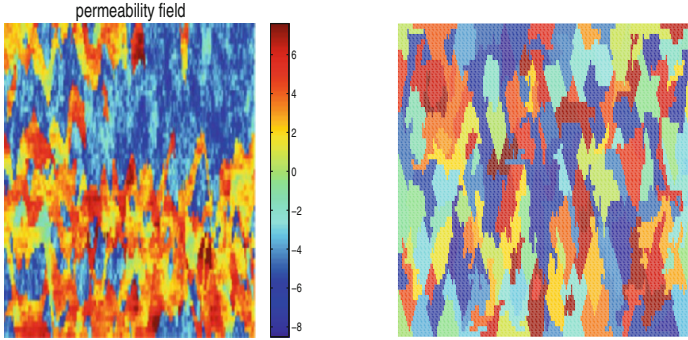
permeability field

Fig. 4.5. 60×220 permeability field and the coarse grid with 180 blocks. A random color is assigned to each coarse-grid block.

reference   multiscale saturation using unstructured grid   multiscale saturation using structured grid
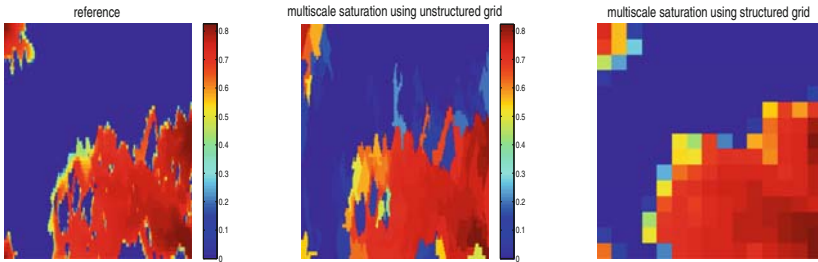
Fig. 4.6. Saturation comparisons.

Table 4.7. Relative L^1 Errors (Layer 65)

Unstruct. Coarse (Number of Blocks)	Sat. Err. (Total)	Sat. Err. (Struct. Grid) (Total)
180	0.0097	0.0130 (10×20)
299	0.0080	0.0125 (15×22)
913	0.0062	0.009 (20×44)

that are aligned in a logical Cartesian fashion where one horizontal layer in the logical grid is assigned to each sedimentary bed to be modeled. In its simplest form, a corner-point grid is specified in terms of a set of vertical or inclined pillars defined over an areal Cartesian 2D mesh in the lateral direction. Each cell in the volumetric corner-point grid is restricted by four pillars and is defined by specifying the eight corner points of the cell, two on each pillar.

We consider only 60 vertical layers of the permeability field. The coarse grid is constructed by subdividing the fine-scale model on 30-by-30-by-60 corner-point cells into 202 coarse-grid blocks. In Figure 4.8, we plot: coarse-grid
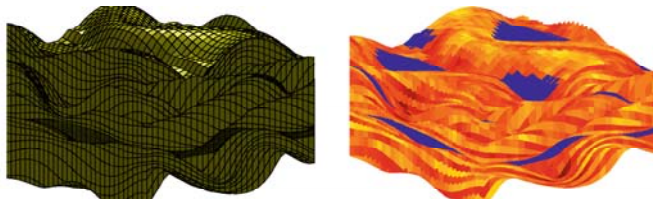
Fig. 4.7. A corner-point model with vertical pillars and 100 layers. To the right is a plot of the permeability field on a logarithmic scale. The model is generated with $SBED^{TM}$, and is courtesy of Alf B. Rustad at STATOIL.
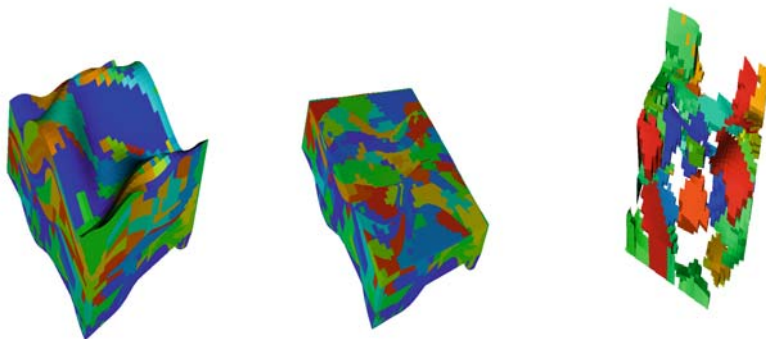

Fig. 4.8. Left: schematic description of unstructured coarsening (each coarse grid block is assigned a random color). Middle: a horizontal slice of unstructured coarsening presented on the left. Right: a coarse grid block (enlarged).

partitioning (left plot) where a random color is assigned to each coarse-grid block; a horizontal slice of coarse partitioning presented on the left plot; and several coarse-grid blocks. In Figure 4.9, we plot the water-cut curves. As we see from this figure, our method provides an accurate approximation of water-cut data. The error that is due to the mixed MsFEM is only 2% (here, we consider L^1 error in the saturation field at PVI = 0.5). We have observed 17% error in the saturation field when both flow and transport equations are solved on the coarse grid. This error is mainly due to the saturation upscaling. The detailed numerical studies when both flow and transport equations are coarsened can be found in [4]. In particular, we show that the errors due to mixed MsFEMs for solving the flow equation are much smaller than the errors due to upscaling of the transport equation. This suggests that more accurate upscaling methods for transport equations are needed. Multiscale methods for transport equations are discussed in Section 5.2.
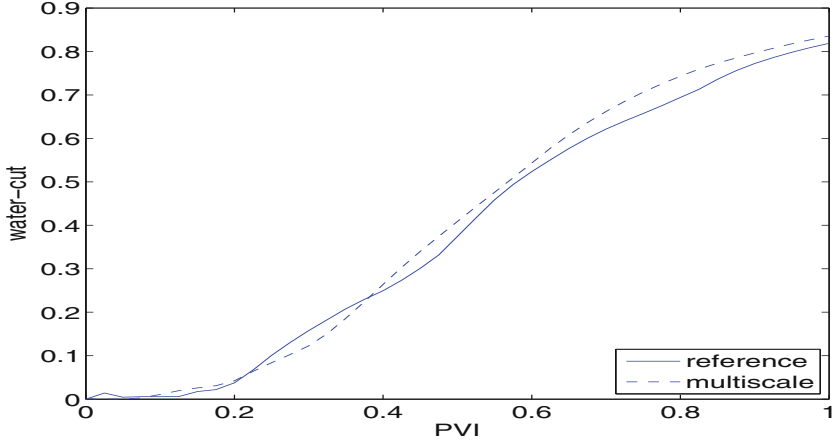
Fig. 4.9. Water-cut for reference and multiscale solutions.

The use of multiple global information in parameter-dependent permeability

In our next set of numerical experiments, we consider a case where one needs to use multiple global fields to construct multiscale basis functions. One can consider this case as a simplified case for the more general stochastic case which is presented in Section 5.7. In our numerical experiments, we consider $k(x, \theta) = \exp(\theta Y(x))$. We investigate a range of θ, $\theta_1 \leq \theta \leq \theta_2$, and use the global single-phase flow solutions corresponding to endpoints $\theta = \theta_1$ and $\theta = \theta_2$ to construct the multiscale basis functions. In particular, $v_1 = -k(x, \theta_1)\nabla p(x, \theta_1)$ and $v_2 = -k(x, \theta_2)\nabla p(x, \theta_2)$ (where $p(x, \theta_1)$ and $p(x, \theta_2)$ solve the global single-phase flow problem) are used to construct mixed multiscale basis functions as described earlier.

In Figure 4.10, the water-cut (which is equal to $1-F$, F being the fractional flow) and the saturation profiles for a value of $\theta = 0.75$ are compared. The global fields corresponding to single-phase flow solutions are computed at $\theta_1 = 0.5$ and $\theta_2 = 1$. The simulations are run with $\mu_o/\mu_w = 5$. We note that the value of θ is different from the values used in generating basis functions. We observe from these figures that the mixed MsFEM provides an accurate representation of the solution. In particular, there is almost no difference in the water-cut curve and the error in the saturation profile at $\mathrm{PVI} = 1$ is less than 5%. This observation is consistent for all other values between θ_1 and θ_2, and it is demonstrated next.

In our next set of numerical experiments, water-cut errors and saturation errors for values of θ between $\theta_1 = 0.5$ and $\theta_2 = 1.5$ are presented. We also compare these results with the results obtained using only one value of θ,
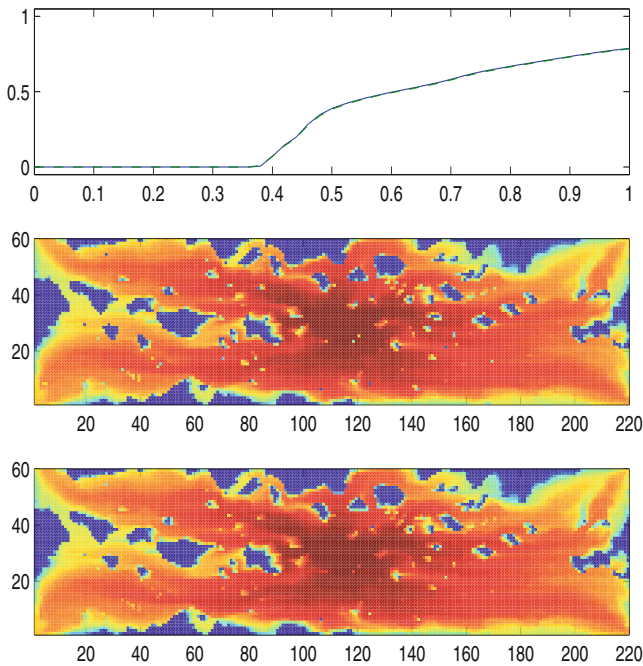
Fig. 4.10. Top: comparison of water-cut between reference solution and multiscale solution; middle: the reference saturation at PVI = 1; bottom: multiscale saturation at PVI = 1 (layer 85).

$\theta = 1$. More precisely, we only use the global solution corresponding to $\theta = 1$ to construct multiscale basis functions. Furthermore, these basis functions are used for solving the two-phase flow on the coarse grid for other values of θ. We observe from Figures 4.11 and 4.12, that the results are substantially better if two global solutions are employed in characterizing the solutions for the entire range of θ. In Figure 4.11, $\mu_o/\mu_w = 0.1$ is taken and in Figure 4.12, $\mu_o/\mu_w = 10$ is taken. It is clear from these figures that the use of two global solutions in mixed MsFEMs gives us an accurate approximation. The presented numerical results show that one can use a few realizations of the permeability field to construct basis functions that can be employed for solving two-phase flow and transport on the coarse grid accurately. Similar ideas have been used in applications of mixed MsFEMs to stochastic equations (see Section 5.7.1).

One of our goals with presented numerical results is to show that the solution can be approximated using multiple global fields. Next, we discuss the numerical convergence of global mixed MsFEMs with limited global information. For this reason, we consider different coarse grids, 6×22, 12×44, and
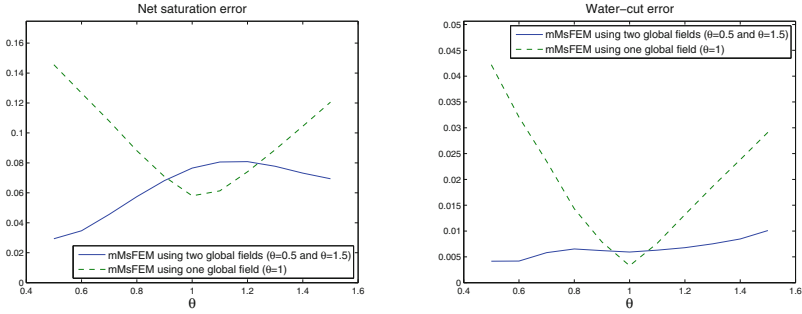
Fig. 4.11. L^1 saturation error and water-cut error using one single-phase flow solution and two single-phase flow solutions, $\mu_o/\mu_w = 0.1$ (layer 85).
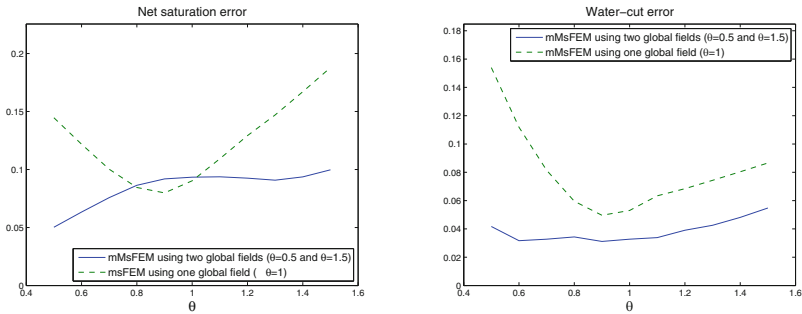

Fig. 4.12. L^1 saturation error and water-cut error using one single-phase flow solution and two single-phase flow solutions, $\mu_o/\mu_w = 10$ (layer 85).

15×55 for the previous example with $\mu_o/\mu_w = 10$. Our convergence analysis (see Section 6.3) indicates that the proposed method converges up to a small parameter that represents how well the two-phase velocity field can be approximated by a single-phase velocity field in each coarse patch. Moreover, the convergence rate also depends on the smoothness of A_i in (4.5). One can consider an ideal toy problem where the convergence rate can be verified by specifying the form of the solution up to smooth functions A_i (see (4.5)). Instead, we would like to consider the SPE 10 example and show that as the coarse mesh size decreases the error decreases. We note that this is in contrast to standard MsFEMs where one can observe the resonance error. As a result, the mixed MsFEM does not converge as h approaches zero. As we see from Figure 4.13, the mixed MsFEM using limited global information converges as the coarse mesh size decreases. This is again an indication that for general complicated media such as SPE 10 with high contrast, one can expect the convergence of mixed MsFEMs using limited global information.

We note that the method can be used for stochastic flow equations. This is presented in Section 5.7.1. In this case, one can take v_i to be the realizations
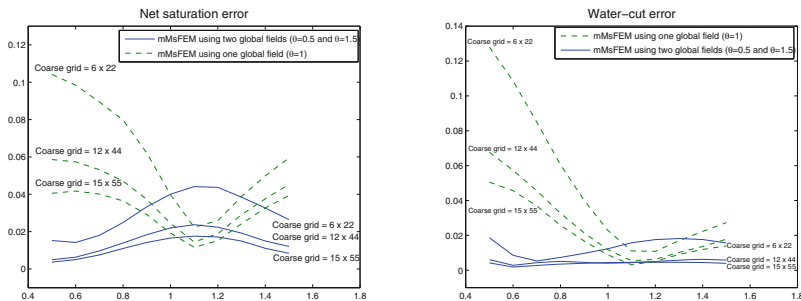
Fig. 4.13. L^1 saturation error and water-cut error using one single-phase flow solution and two single-phase flow solutions, $\mu_o/\mu_w = 10$ for different degrees of coarsening (layer 85).

of the random fields. This way multiscale basis functions capture the small-scale information across the realizations of stochastic porous media equations. Because these approaches do not necessarily require global information and can be considered as an application of MsFEMs, we present them in the last chapter of the book.

4.3 Galerkin multiscale finite element methods using limited global information

4.3.1 A special case

First, we consider a special case where only one global field is used for generating multiscale basis functions. We denote the solution of the pressure equation at time zero by $p^{sp}(x)$, where the superscript sp refers to single-phase flow ($\lambda = 1$ in (4.1)). In defining $p^{sp}(x)$, we use the actual boundary conditions of the global problem. The boundary conditions for modified basis functions are defined in the following way. For simplicity of the presentation, we consider a rectangular partition in 2D. For each rectangular element K with vertices x_i ($i = 1, 2, 3, 4$), denote by $\phi_i(x)$ a restriction of the nodal basis on K, such that $\phi_i(x_j) = \delta_{ij}$. At the edges where $\phi_i(x) = 0$ at both vertices, we take the boundary condition for $\phi_i(x)$ to be zero. Consequently, the basis functions are localized. We only need to determine the boundary condition at two edges that have the common vertex x_i ($\phi_i(x_i) = 1$). Denote these two edges by $[x_{i-1}, x_i]$ and $[x_i, x_{i+1}]$ (see Figure 4.14). We only need to describe the boundary condition $g_i(x)$ for the basis function $\phi_i(x)$ along the edges $[x_i, x_{i+1}]$ and $[x_i, x_{i-1}]$. If $p^{sp}(x_i) \neq p^{sp}(x_{i+1})$, then

$$g_i(x)|_{[x_i, x_{i+1}]} = \frac{p^{sp}(x) - p^{sp}(x_{i+1})}{p^{sp}(x_i) - p^{sp}(x_{i+1})}, \quad g_i(x)|_{[x_i, x_{i-1}]} = \frac{p^{sp}(x) - p^{sp}(x_{i-1})}{p^{sp}(x_i) - p^{sp}(x_{i-1})}.$$
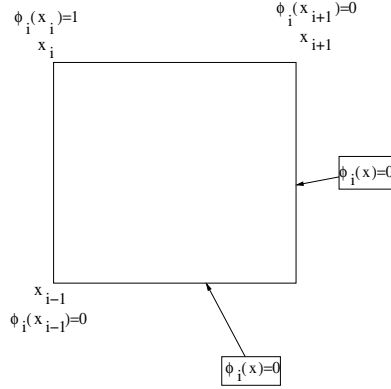
Fig. 4.14. Schematic description of nodal points.

If $p^{sp}(x_i) = p^{sp}(x_{i+1}) \neq 0$, then

$$g_i(x)|_{[x_i, x_{i+1}]} = \phi_i^0(x) + \frac{1}{2p^{sp}(x_i)}(p^{sp}(x) - p^{sp}(x_{i+1})),$$

where $\phi_i^0(x)$ is a linear function on $[x_i, x_{i+1}]$ such that $\phi_i^0(x_i) = 1$ and $\phi_i^0(x_{i+1}) = 0$. Similarly,

$$g_{i+1}(x)|_{[x_i, x_{i+1}]} = \phi_{i+1}^0(x) + \frac{1}{2p^{sp}(x_{i+1})}(p^{sp}(x) - p^{sp}(x_{i+1})),$$

where $\phi_{i+1}^0(x)$ is a linear function on $[x_i, x_{i+1}]$ such that $\phi_{i+1}^0(x_{i+1}) = 1$ and $\phi_{i+1}^0(x_i) = 0$. If $p^{sp}(x_i) = p^{sp}(x_{i+1}) \neq 0$, then one can also use simply linear boundary conditions. If $p^{sp}(x_i) = p^{sp}(x_{i+1}) = 0$ then linear boundary conditions are used. Finally, the basis function $\phi_i(x)$ is constructed by solving the leading-order homogeneous equation $\operatorname{div}(k\nabla\phi_i) = 0$. The choice of the boundary conditions for the basis functions is motivated by the analysis. In particular, we would like our basis functions to span the fine-scale solution $p^{sp}(x)$. Using this property and Cea's lemma one can show that the pressure obtained from the numerical solution is equal to the underlying fine-scale pressure. The latter combined with the fact that the two-phase flow solution p is a smooth function of p^{sp} (see [103]) allows us to show that the proposed multiscale finite element method converges independent of resonance error. This approach is effective when the solution of (4.1) is a smooth function of p^{sp}.

4.3.2 General case

The MsFEMs considered above employ information from only one single-phase flow solution. In general, it might be necessary to use information from multiple global solutions for the computation of an accurate two-phase flow

solution. The previous MsFEMs can be extended to take into account additional global information. Next, we present an extension of the Galerkin MsFEM that is based on the partition of unity method [32] (also see e.g., [248], [121], [153]).

As we mentioned before, we assume (4.2); that is $\|p - G(p_1, ..., p_N)\|_{L^2(\Omega)}$ is sufficiently small for a priori selected global fields $p_1, ..., p_N$. Here G is a smooth function. Here, $p_1, ..., p_N$ are global (or local) fields that can approximate the solution.

Let ω_i be a coarse-grid patch (see Figure 4.15), and define ϕ_i^0 to be partition of unity functions (e.g., piecewise linear basis functions) such that $\phi_i^0(x_j) = \delta_{ij}$. For simplicity of notation, denote $p_1 = 1$. Then, the MsFEM for each patch ω_i is constructed by

$$\Psi_{ij} = \phi_i^0 p_j,$$

where $j = 1, .., N$ and i is the index of nodes (see Figure 4.15). We note that in each coarse patch $\sum_{i=1}^{n} \Psi_{ij} = p_j$ is the desired global field. Because the solution can be approximated by p_j, one can show that the MsFEM converges independent of resonance errors ([162]). Note that the form of the function G is not important for the computations; however, it is crucial that the basis functions span $p_1, ..., p_N$ in each coarse block. The convergence results are presented in Section 6.3.
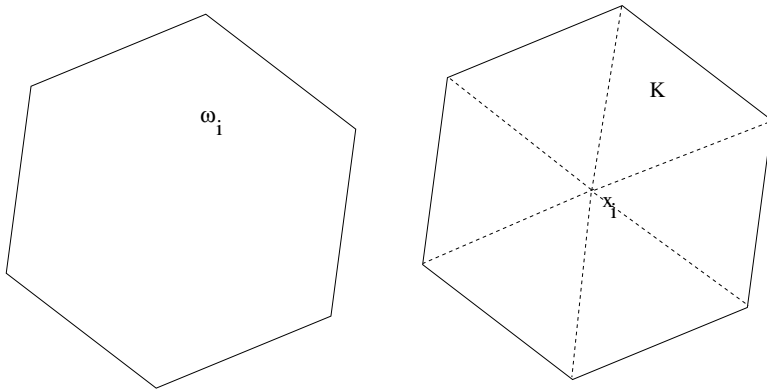

Fig. 4.15. Schematic description of patch.

4.3.3 Numerical results

Next, we show numerical results obtained for MsFEMs using limited global information presented in Section 4.3.1. We consider two-phase flow and transport and use only one global field, single-phase flow information ($N = 1$), as
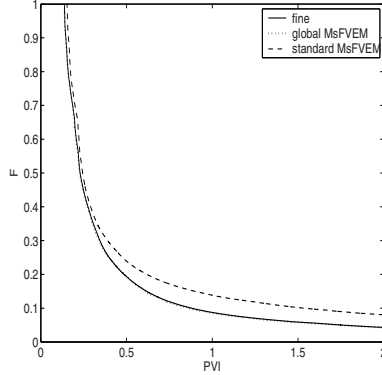
Fig. 4.16. Fractional flow comparison for standard MsFVEM and global MsFVEM.

described in Section 4.3.1 in the construction of basis functions. The basis functions are coupled via the finite volume formulation of the problem (see Section 2.5.1). We refer to this method as the global MsFVEM. Our first numerical example is for the permeability layer depicted in Figure 4.1 and two-phase flow parameters presented earlier in Section 2.10. As before, we specify $p = 1$, $S = 1$ along the $x = 0$ edge and $p = 0$ along the $x = 5$ edge. On the rest of the boundaries, we assume a no-flow boundary condition. Results are also presented in terms of the fraction of oil in the produced fluid (i.e., oil-cut, designated by F) against pore volume injected (PVI). Recall that PVI represents dimensionless time and is computed via $\int Q dt / V_p$, where V_p is the total pore volume of the system and Q is the total flow rate (see (2.44) for the definition of PVI).

In Figure 4.16, the fractional flows are plotted for standard and global MsFVEMs. We observe from this figure that the global MsFVEM is more accurate and provides nearly the same fractional flow response as the direct fine-scale calculations. In Figure 4.17, we compare the saturation fields at PVI = 0.5. As we see, the saturation field obtained using the global MsFVEM is very accurate and there is no longer the saturation pocket at the left bottom corner (cf. Section 4.1.1). Thus, the global MsFVEM captures the connectivity of the media accurately.

In the next set of numerical results, we test global MsFVEMs for a different layer (layer 40) of the SPE comparative solution project. In Figures 4.18 and 4.19, the fractional flows and total flow rates (Q) are compared for two different boundary conditions. One can see clearly that the global MsFVEM gives nearly exact results for these integrated responses. The standard MsFVEM tends to overpredict the total flow rate at time zero. This initial error persists at later times. This phenomenon is often observed in the upscaling of two-phase flows. More numerical results and discussions can be found in [103]. These numerical results demonstrate that global MsFEMs which use limited
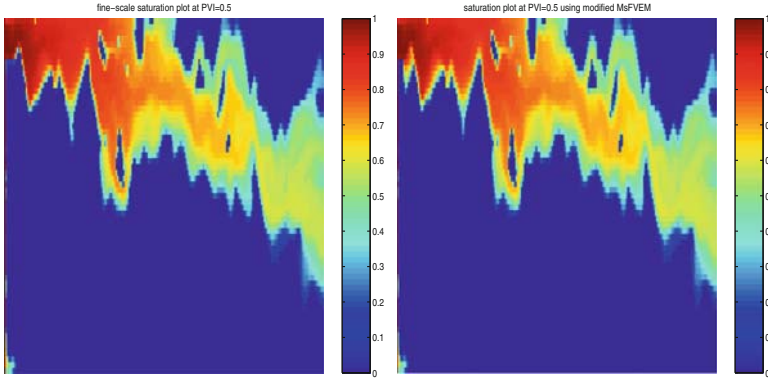
Fig. 4.17. Saturation maps at PVI = 0.5 for fine-scale solution (left figure) and global MsFVEM (right figure).
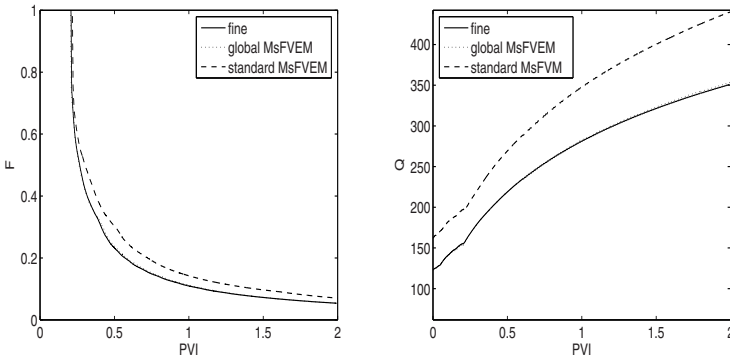

Fig. 4.18. Fractional flow (left figure) and total production (right figure) comparison for standard MsFVEM and global MsFVEM (layer 40).

global information are more accurate. Moreover, global MsFEMs are capable of capturing long-range flow features accurately for channelized permeability fields.

In the next set of numerical results, we consider another layer of the upper Ness (layer 59). In Figure 4.20, both fractional flow (left figure) and total flow (right figure) are plotted. We observe that the global MsFVEM gives almost the exact results for these quantities, whereas the standard MsFVEM overpredicts the total flow rate, and there are deviations in the fractional flow curve around PVI ≈ 0.6. Note that unlike the previous case, fractional flow for standard MsFVEM is nearly exact at later times (PVI ≈ 2). In Figure 4.21, the saturation maps are plotted at PVI = 0.5. The left figure represents the fine scale, the middle figure represents the results obtained using a standard MsFVEM, and the right figure represents the results obtained using a global
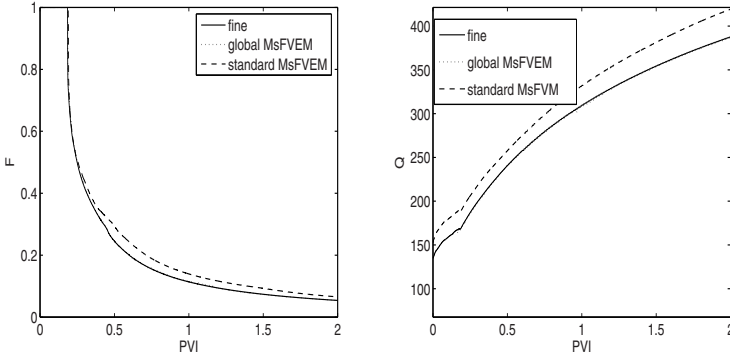
Fig. 4.19. Fractional flow (left figure) and total production (right figure) comparison for the standard MsFVEM and global MsFVEM (layer 40).
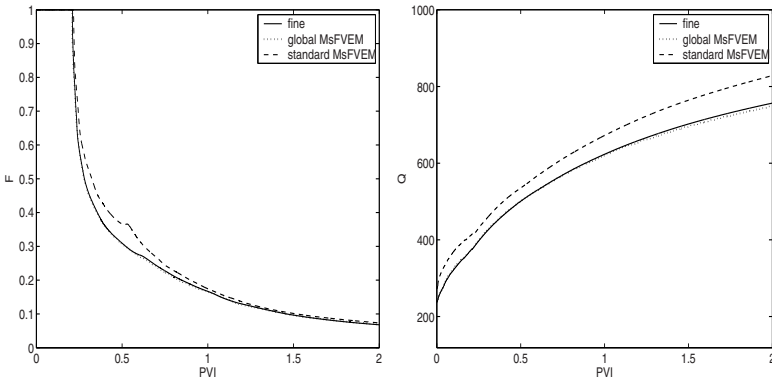

Fig. 4.20. Fractional flow (left figure) and total production (right figure) comparison for the standard MsFVEM and global MsFVEM.

MsFVEM. We observe from this figure that the saturation map obtained using a standard MsFVEM has some errors. These errors are more evident near the lower left corner. The results of the saturation map obtained using the global MsFVEM are almost the same as the fine-scale saturation field. It is evident from these figures that the global MsFVEM performs better than the standard MsFVEM.

4.4 The use of approximate global information

In the above discussions, the global fields are computed by solving simplified fine-scale equations. One can also use approximate global solutions instead of solving fine-scale elliptic equations. There are various ways one can attempt to
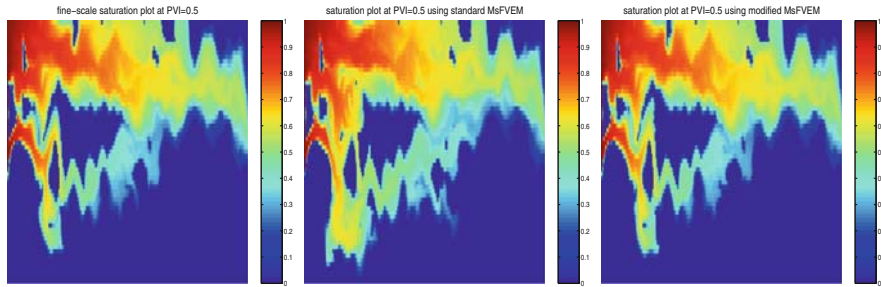
Fig. 4.21. Saturation maps at PVI = 0.5 for fine-scale solution (left figure), standard MsFVEM (middle figure), and global MsFVEM (right figure).

approximate the global fields and we briefly discuss two types of approximate global solutions. In the first approach, approximate global fields that capture nonlocal effects are computed iteratively. In the second approach, we attempt to compute global fields with fewer fine-scale details by homogenizing some small-scale features that can be localized.

4.4.1 Iterative MsFEM

One can attempt to capture nonlocal effects iteratively by using the approximate solutions obtained from MsFEMs. This procedure is schematically presented in Figure 4.22. At each iteration, approximations of the global solutions obtained via MsFEMs are used in the computation of multiscale basis functions. The computations of multiscale basis functions are the same as discussed above (e.g., (4.6)). Once the basis functions are computed, the global problem is solved on the coarse grid and updated approximations of the global solutions are computed. These global solutions are again used for multiscale basis function computation after possible post-processing with smoothers if needed. A convergence criterion based on the difference of consecutive approximate MsFEM solutions can be used to stop the iterations. In order to avoid using the same space of multiscale basis functions, one can use different sizes of oversampling domains in the computation of basis functions.

   An algorithm with a similar concept was introduced in [93]. In [93], the authors proposed the use of a MsFVEM solution as a global solution. Numerical results show that one can achieve substantial improvement when small oversampling is employed in computing the global solutions. Moreover, one can apply this approach iteratively, by re-computing the MsFVEM solution. This iterative procedure converges in two to three iterations for heterogeneous permeability fields such as SPE 10. In general, the correction to the multiscale solution via iterations can be very useful in many practical applications. Indeed, computing a global solution each time when heterogeneities or flow fields change can be expensive. On the other hand, the iterative approaches that can compute the approximate global solution by updating a few
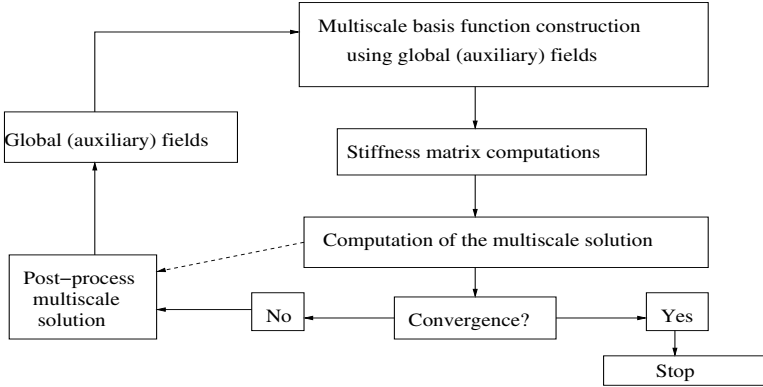
Fig. 4.22. An outline of iterative MsFEM.

multiscale basis functions can be very useful in fast flow simulations. These approaches share some similarities with domain decomposition methods (e.g., [137]), although there are important differences. The approach proposed in [93] iteratively computes multiscale basis functions that can be re-used for different source terms and boundary conditions, and domain decomposition methods correct the solution in the iterations. One can also keep multiscale basis functions the same during the iterations and compute the corrections to the solution in the iterations.

4.4.2 The use of approximate global information

Another possible approximation of global solutions can be obtained by removing the small-scale details that can be localized. This way, one will compute only important nonlocal features of the global fields by homogenizing some of the small-scale features that can be recovered in the basis function construction (see Figure 4.23 for the illustration). This can provide CPU savings in global solution computations because not all small-scale features are resolved. To demonstrate this concept, we assume that the coefficients are described by $k_{\delta^>,\epsilon}(x)$, where $\delta^>$ refers to the hierarchy of scales that are larger than δ, and the parameter ϵ ($\epsilon \ll \delta$) refers to the small scale that can be homogenized. Denote the partially homogenized coefficients by $k^*_{\delta^>}(x)$. By homogenizing ϵ scales, one can use $k^*_{\delta^>}(x)$ to compute the global fields. The use of nonuniform coarsening will allow us to discretize the equation with the coefficients $k^*_{\delta^>}(x)$ on a coarser grid compared to the equation with the coefficients $k_{\delta^>,\epsilon}(x)$. Indeed, many fine-scale features are due to ϵ scales. This will provide CPU savings in the computation of auxiliary global fields. Moreover, one can use smaller regions (RVE) as in Section 2.6 in the computation of $k^*_{\delta^>}(x)$. In [108], we use the global solutions computed with the coefficients $k^*_{\delta^>}(x)$ to construct multiscale basis functions and investigate the convergence of the method.
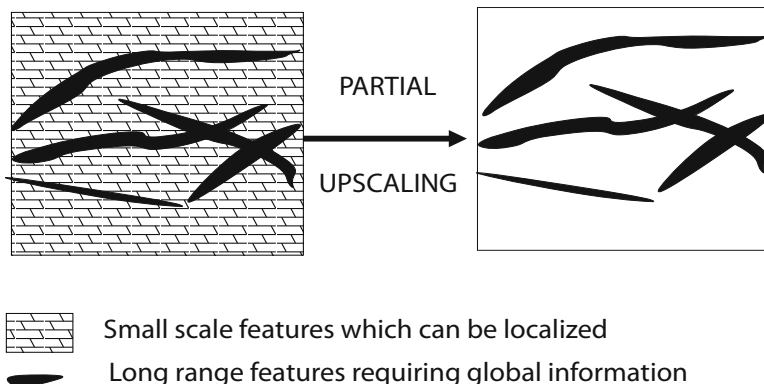
Small scale features which can be localized

Long range features requiring global information

Fig. 4.23. Schematic description of partial upscaling.

4.5 Discussions

One of the theoretical works on using limited global information in MsFEMs is by Owhadi and Zhang [218]. In this work, the authors show that the solution is smooth in a harmonic coordinate system. These results are shown under some suitable assumptions for the case $d = 2$ and more restrictive assumptions for the case $d = 3$. The use of harmonic coordinates in homogenization is not new. In [169], the author used harmonic coordinates to transform the elliptic equations with random coefficients into the elliptic equations in non-divergence forms (without lower-order terms). The homogenization of elliptic equations in non-divergence form is carried out by using spatial averaging. Harmonic coordinates in [218] consist of directional solutions of the single-phase flow equation. This suggests that one can solve the flow equation with an arbitrary right-hand side or smooth mobility $\lambda(x)$ in a harmonic coordinate system using standard finite element basis functions on a coarse grid. In the original (physical) coordinate system, this method entails solving the flow equations with multiscale basis functions that span the global solutions and, perhaps, constant or low-order polynomials. Moreover, the coarse grid in the original coordinate system is the image of the regular coarse-grid block in the harmonic coordinate system. This image is taken under the inverse of harmonic coordinate transformation. These coarse-grid blocks are usually highly distorted [218].

The multiscale methods using limited global information usually perform well (numerically) for high-contrast media. However, rigorous analysis for general high-contrast media is still an open question. Some results along this direction have been obtained recently in [137, 76, 67]. In [76], piecewise constant heterogeneities are considered. The authors show that by constructing some appropriate multiscale boundary conditions for the basis functions that take into account the local geometric property of the solution, the MsFEM converges with an optimal convergence rate independent of the aspect ratio

of the heterogeneous coefficient. This is perhaps the first result in which one can obtain an optimal convergence rate independent of the high-contrast of the coefficients for a finite element method which does not require alignment of the finite element mesh with the interface boundary. In [67], the high contrast problem is formulated as an interface problem without a high contrast. Then the basis functions for the interface on the coarse grid are computed in addition to regular multiscale basis functions.

The question of whether local changes in the permeability can be treated by modifying multiscale basis functions locally is addressed in [77]. The authors consider the mobility functions $\lambda(S)$ in (4.1) which are discontinuous functions. It is shown that by changing the basis functions only near the discontinuities, one can achieve a convergent method for problems without scale separation.

The limited global information can be very useful in coarsening. In [218], the authors use the level sets of the directional solutions to generate the coarse grid. The use of level sets of the directional solutions has limitations. In previous findings, the pressure-streamline coordinates have been used in coarsening. In a recent work [93], we propose a generic algorithm, extending the main idea of [69], for performing nonuniform coarsening using a single-phase velocity field. We show that one can achieve higher accuracy with fewer degrees of freedom (compared to uniform coarsening).

As we mentioned earlier the use of limited global information in coarsening is not new. The single-phase information has been used in upscaling methods for porous media flows before. One of the main difficulties in upscaling methods when using limited global information is to recover exactly the average response of the global fine-scale information. In [140], the authors solve an optimization problem for computing the upscaled permeabilities that give nearly the same average response as the global solution. In [69], the authors propose an iterative method using global information which converges in a few iterations. The resulting upscaled coefficients give nearly the same average flow response as the global single-phase flow solution. Limited global information is also used in multiphase upscaling for upscaling of relative permeabilities.

As we mentioned above one can use multiple global solutions in computing basis functions. This is particularly useful for stochastic problems, where different realizations are used in computing basis functions, or in the situations where a priori knowledge about the change in heterogeneities or boundary conditions is known. Then, multiple global solutions can be used in constructing multiscale basis functions. In this way, one can use the same set of basis functions throughout the simulation.

We would like to note that the use of limited global information in nonlinear problems does not seem to be possible, in general. This is due to the fact that the heterogeneities depend on nonlinearities and the solution. The use of limited global information usually assumes knowledge about the spatial heterogeneities. For nonlinear problems, one does not have a priori knowledge about the heterogeneities. One approach is to identify a set of hetero-

geneities that will occur in nonlinear problems. For example, in nonlinear elliptic or parabolic problems, this will involve finding spatial information about $k(x, p, \nabla p)$ for all p. Once this has been determined, one can construct a larger set of basis functions that are capable of capturing all the long-range effects. To our best knowledge, these issues have not been addressed so far.

Finally, we mention that the multiscale methods using limited global information can be extended to other linear equations, such as wave equations [163].